Available online at www.sciencedirect.com

ScienceDirect

Energy Procedia 137 (2017) 452–459

Energy Procedia

www.elsevier.com/locate/procedia

14th Deep Sea Offshore Wind R&D Conference, EERA DeepWind'2017, 18-20 January 2017, Trondheim, Norway

A step towards reduced order modelling of flow characterized by wakes using Proper Orthogonal Decomposition

Eivind Fonn[a,*], Mandar Tabib[a], M. Salman Siddiqui[a,b], Adil Rasheed[a], Trond Kvamsdal[a,b]

[a] *CSE Group, Mathematics and Cybernetics, Sintef Digital, 7034, Trondheim, Norway*
[b] *Department of Mathematical Sciences, NTNU, Alfred Getz vei 1, 7491, Trondheim, Norway*

Abstract

High fidelity simulations of flow can be quite demanding, involving up to $O(10^6)$ to $O(10^9)$ degrees of freedom, and several hours or days of computational time, even on powerful parllel architectures. These techniques become prohibitive when expected to deal quickly and efficiently with repetitive solutions of partial differential equations. One set of PDE encountered on a regular basis is the Navier Stokes equation, used to simulate flow around complex geometries, e.g. sub-sea structures. To address the issues associated with computational efficiency, the field of Reduced Order Modelling (ROM) is evolving quickly. In this paper, we investigate the use of Proper Orthogonal Decomposition (POD) as a potential method for constructing reduced bases for such ROMs. In the case of flow around cylindrical bodies and the NACA 0015 airfoil we found that only a few modes were sufficient to represent the dominant flow structures and their associated energies. This makes POD an attractive candidate for constructing such bases.

Peer-review under responsibility of SINTEF Energi AS.

Keywords: Reduced Order Modelling; ROM; Partial Orthogonal Decomposition; POD; Reduced Basis

1. Introduction

Numerical methods and tools to simulate flow around complex geometries like wind turbines and sub-sea structures have evolved significantly in recent years. However, their usage typically requires access to high performance computing facilities, which are not always possible. Consequently, there is an ever-increasing demand for computationally efficient desktop tools that can be used for design and real-time control and management systems. These requirements are diametrically opposed to those of the high fidelity simulation tools availableat our disposal.

For flow simulations, the governing equations are the Navier Stokes equations, which are written in terms of certain input parameters whose effect one might want to investigate. For this sort of problem, *reduced order modelling* (ROM) is a generic term used to identify any approach aimed at replacing the high fidelity problem with one featuring a much lower numerical complexity. The key to the success of any ROM is the ability to evaluate the solution to this reduced

* Corresponding author. Tel.: +47-4144-9889.
E-mail address: eivind.fonn@sintef.no

1876-6102
Peer-review under responsibility of SINTEF Energi AS.
10.1016/j.egypro.2017.10.369

problem at a cost (usually in terms of computational time) that is independent of the dimension of the original high-fidelity problem.

Reduced basis methods represent one notable instance of ROM techniques [1]. They exploit the parametric dependence of the solution by combining a handful of high fidelity simulations (*snapshots*) computed *a priori* for a small set of parameter values. This way, a large linear system is replaced by a much smaller one, whose dimension is related to the number of snapshots. The key, then, is to construct such reduced bases. One method that can be used, and which is investigated in the following, is *proper orthogonal decomposition* (POD). The workflow requires a number of modules, each of which are described below.

1. High fidelity simulation module: This module is used for conducting high fidelity simulations of flow around sub-sea structures (in this case, a cylinder) for varying inlet boundary conditions. It is based on the OpenFOAM (OF) framework.
2. Data storage and processing module: High fidelity simulation results (i.e. snapshots) are potentially huge in size and requires efficient storage and processing. The results, generally conducted on onstructurede meshes in VTK format are firsted interpolated on structured meshes. These are then converted to HDF5 (*Hierarchical Data Format version 5*) and NetCDF4 (*Network Common Data Form version 4*) formats, and are made available via an OPeNDAP server (*Open-source Project for a Network Data Access Protocol*). This obviates the need to duplicate data on multiple computers for further processing.
3. Proper orthogonal decomposition module: This module consists of routines for conducting POD and constructing the reduced bases.

2. Module description

A more technical description of the modules is provided in the following subsections.

2.1. High fidelity simulation module

A transient 3D computational fluid dynamics (CFD) model is utilized. The model computes velocity, pressure and turbulence fields. The turbulence is modeled using a one-equation sub-grid scale (SGS) turbulent kinetic energy LES model. The equations for LES are derived by applying filtering operator to the Navier-Stokes equations. The filtering results in (1) and (2).

$$\frac{\partial \overline{u}_i}{\partial t} = 0, \tag{1}$$

$$\frac{\partial \overline{u}_i}{\partial t} + \frac{\partial}{\partial x_j}(\overline{u}_i \overline{u}_j) = -\frac{\partial \overline{p}}{\partial x_i} - \frac{\partial B_{ij}}{\partial x_j} + \nu \frac{\partial 2\overline{u}_i}{\partial x_j \partial x_j}, \tag{2}$$

where $\overline{u}_i$ is the filtered (or resolved) velocity, $\overline{p}$ the filtered pressure, ν the dynamic viscosity and

$$B_{ij} = \overline{u_i u_j} - \overline{u}_i \overline{u}_j. \tag{3}$$

The term $\boldsymbol{B}$ can be modeled using (4)

$$\boldsymbol{B} = \frac{1}{3}\,\mathrm{Tr}(\boldsymbol{B})\boldsymbol{I} + \nu_{\mathrm{sgs}}(\nabla \boldsymbol{u} + \nabla^{\intercal}\boldsymbol{u}) \tag{4}$$

where $\mathrm{Tr}(\boldsymbol{B})$ stands for the trace of the tensor $\boldsymbol{B}$, $\boldsymbol{I}$ is the identity matrix, and ν_{sgs} is the so called SGS viscosity, which is expressed in terms of the subgrid turbulent kinetic energy k_{sgs} using (5).

$$\nu_{sgs} = (C_k \Delta) k_{sgs}^{1/2} \tag{5}$$

where $C_k = 0.094$. k_{sgs} is computed using its transport (6).

$$\frac{\partial k_{\mathrm{sgs}}}{\partial t} + \frac{\partial \overline{u}_i k_{\mathrm{sgs}}}{\partial x_i} = 2\nu_{\mathrm{sgs}} |\overline{D}_{ij}|^2 - C_e \frac{k_{\mathrm{sgs}}^{3/2}}{\Delta} + \frac{\partial}{\partial x_i}\left(\nu_{\mathrm{sgs}} \frac{\partial k_{\mathrm{sgs}}}{\partial x_i}\right) + \nu \frac{\partial^2 k_{\mathrm{sgs}}}{\partial x_i \partial x_i} \tag{6}$$

where $\overline{D}_{ij}$ is the filtered rate of strain tensor, and $C_e = 1.048$ is a constant.

To ensure continuity, an elliptic equation for the modified pressure is created by combining the continuity equation with the divergence of momentum equation. This elliptic equation along with the momentum equation and sub-grid scale turbulent kinetic energy equation are solved in a segregated manner using the PISO-SIMPLE (*PIMPLE*) algorithm. This ensures use of a higher time step for transient simulations. OpenFOAM uses a finite volume discretization technique, wherein all equations are integrated over control volumes (CV) using the Green-Gauss divergence theorem. This theorem converts the volume integral of the divergence of a variable into a surface integral of the variable itself over faces comprising the CV. Thus, the divergence term defining the convection terms can be computed using the face values of variables in the CV. These face values are obtained from their neighboring cell-centered values by using a convective scheme. In this work, all equations (except k_{sgs}) use second order linear discretization scheme, while the turbulent equations use a blend of linear-upwind convection schemes. Similarly, the diffusion term involving the Laplacian operator (the divergence of the gradient) is simplified to computing the gradient of the variable at the face. The gradient term can be split into contributions from the orthogonal and the non-orthogonal parts, and both these have been accounted for. This module has been used in the past to simulate flow in complex terrain (see [2–4]) and flow around rotating turbines [5] within the FSI-WT project [6].

2.2. Data storage and processing module

For processing the potentially large amounts of data from the high fidelity simulations, it is desirable to achieve a networked workflow. This should minimize the strain on the local disk, as well as duplication of effort among users.

To this end, an OPeNDAP server was set up. OPeNDAP is a data transport protocol based on HTTP (*Hyper Text Transfer Protocol*), allowing a central server to serve common data storage formats (for example NetCDF4, HDF5), so that clients can read only what they need and when they need it. As long as the client-side accessing library is well written, for the end user this should be functionally identical to reading local files.

No support is available for serving VTK files in this manner. However, since OPeNDAP is built on HTTP, it ignores files which it does not understand, VTK among them. This makes it possible to write a "naive" wrapper for VTK, which downloads the complete data of the file to a temporary location and opens it instead.

2.3. Proper orthogonal decomposition module

Given an ensemble of solutions to a problem $\{\varphi_i\}_{i=1}^{p}$ (evaluated at different timesteps, say), each adjusted to have mean zero[1], we seek a set of orthogonal modes $\{\zeta_j\}_{j=1}^{p}$ such that the reconstructed ensemble

$$\varphi_i^N = \sum_{j=1}^{N} a_i^j \zeta_j$$

truncated at order N can represent to some reasonable degree the original ensemble. Assuming also that the original ensemble represents a "typical" set of solutions to the given problem, one might hope that $\{\zeta_j\}_{j=1}^{N}$ gives an appropriate basis and function space for the sparse representation of such solutions.

The method of proper orthogonal decomposition (POD), also known as principal component analysis (PCA) provides a well tested mechanism for this. The closeness of approximation should be measured in some norm $\|\cdot\|_a$, and the square of this norm corresponds to the statistical notion of variance. The inner product $\langle\cdot,\cdot\rangle_a$ that induces the norm corresponds to covariance. The covariance matrix is then

$$C_{ij} = \frac{1}{N}\left\langle \varphi_i, \varphi_j \right\rangle_a .$$

Its eigenpairs $(\boldsymbol{q}_i, \lambda_i)$ give the modes ζ_i according to

$$\zeta_i = \frac{1}{\sqrt{\lambda_i}} \sum_j q_i^j \varphi_j .$$

[1] Centering data around the mean is necessary for the eigenvalue decomposition to capture *variance* rather than *means* in the first modes. Although in a statistical context the covariance matrix is centered by definition, in the present formulation it is not.

It can be seen that if the eigenvectors $\boldsymbol{q}_i$ of $\boldsymbol{C}$ are chosen to be ortonormal, i.e. $\boldsymbol{q}_i^\intercal \boldsymbol{q}_j = \delta_{ij}$, then ζ_i are orthonormal in the a-inner product, viz.

$$\left\langle \zeta_i, \zeta_j \right\rangle_a = \frac{1}{\sqrt{\lambda_i \lambda_j}} \boldsymbol{q}_i^\intercal \boldsymbol{C} \boldsymbol{q}_j = \sqrt{\frac{\lambda_j}{\lambda_i}} \delta_{ij} = \delta_{ij}.$$

The sum of eigenvalues is equal to the trace of $\boldsymbol{C}$, and thus can be interpreted as the average variance in the ensemble. In particular, each individual eigenvalue λ_i is equal to the average variance captured by its corresponding mode throughout the ensemble. Therefore the truncation order N should be chosen such that

$$\frac{\sum_{i=N+1}^{p} \lambda_i}{\sum_{i=1}^{p} \lambda_i} \leq \epsilon$$

for some predetermined level of tolerance ϵ, and it is hoped that suitably low ϵ still yield N such that $N(\epsilon) \ll p$. In the remainder of this work we have chosen to focus on the represenation of *velocity*. Thus the covariance function can be written

$$\left\langle (\overline{\boldsymbol{u}}_i, p_i), (\overline{\boldsymbol{u}}_j, p_j) \right\rangle_a = \int_\Omega \overline{\boldsymbol{u}}_i \cdot \overline{\boldsymbol{u}}_j,$$

Where a solution φ_i in this case has been identified with its velocity and pressure solutions $\boldsymbol{v}_i$ and p_i. A more appropriate choice for representing both velocity *and* pressure are covariance functions of the form

$$\left\langle (\overline{\boldsymbol{u}}_i, p_i), (\overline{\boldsymbol{u}}_j, p_j) \right\rangle_a = \int_\Omega \left(\overline{\boldsymbol{u}}_i \cdot \overline{\boldsymbol{u}}_j + c p_i p_j \right),$$

where an appropriate scaling constant c must be chosen to make the two quantities comparable, e.g.

$$c = \frac{\sum_i \|\overline{\boldsymbol{u}}_i\|^2}{\sum_i \|p_i\|^2}.$$

3. Snapshot generation

To generate snapshots, LES simulations of flow around a circular cylinder were conducted at three different Reynolds numbers (based on cylinder diameter and bulk inlet velocity) of Re = 265, Re = 2580 and Re = 40000. In addition to three simulations with uniform inlet velocity, three simulations with pulsating inflow boundary conditions were also conducted. The diameter (D) of the cylinder is 1 m. The bulk or free-stream inlet velocity (U_∞) is 1 m/s for the uniform inflow case. The pulsating inflow was provided using (7).

$$U(t) = U_\infty + \Delta U \sin(2\pi f t) \tag{7}$$

As per suggestion by [7], the values of ΔU and f are selected so that the parameter $\epsilon = \frac{\Delta U}{2\pi f D}$ is around 0.2. This ensures a sufficiently a large threshold window for lock-on to occur [8]. The Reynolds number is changed by varying the fluid viscosity. These three Reynolds numbers represent different physical regimes. The domain size is $40D \times 20D \times 1D$ in the streamwise (X), flow normal (Y) and spanwise (Z) directions. A periodic boundary condition is applied in the spanwise direction while a slip boundary condition is applied in the flow-normal direction. The inlet (on left) and outlet (on right) boundaries are specified along the streamwise direction. The cylinder is placed such that its centre is $10D$ from the inlet plane and the outlet plane is located $30D$ downstream from the centre. For Re = 2580 and Re = 40000, the hexahedrally dominated mesh is of size about 7.2×10^6 cells, with the region around the cylinder and downstream of the vortex shedding path being highly refined. The mesh element size range from $0.003D$ close to the cylinder surface (resulting in $y^+ < 1$) to $0.5D$ furthest away from the cylinder surface in the computational domain. Details on domain set up, mesh resolution, boundary conditions and physical interpretation of results can be found in [8]. More details regarding the physical interpretation of the results can be found in [7,9]. We have intentionally omitted similar discussion here since, our objective in this paper is to just evaluate the applicability of ROM using POD.

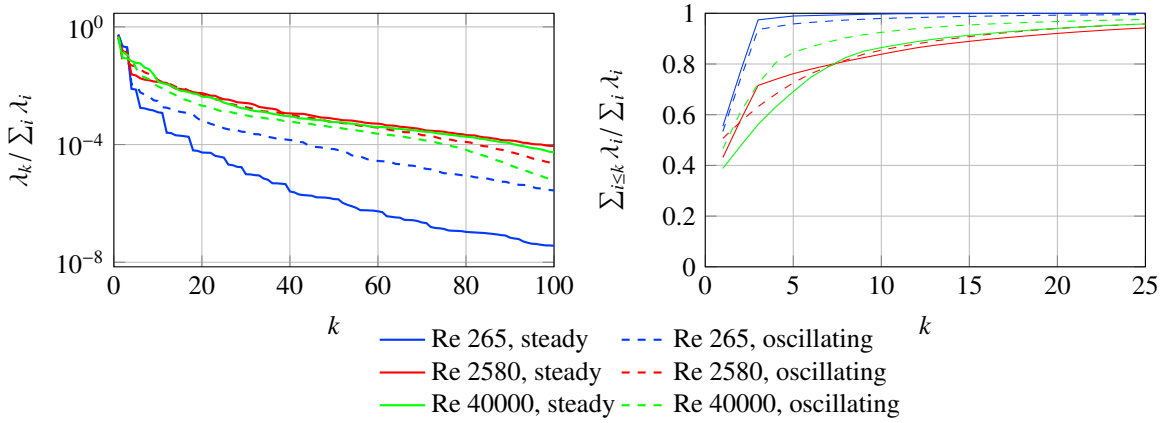

Fig. 1. Energy spectra (on the left, up to 100 eigenvalues) and cumulative energy spectra (on the right, up to 25 eigenvalues) of all six cylinder cases.

To further validate the potential of the method, snapshots were also generated from a high fidelity simulation of flow around a NACA 0015 airfoil at an attack angle of 17°. RANS simulations were performed at the Reynolds number of $\mathrm{Re} = 2 \times 10^4$, $\mathrm{Re} = 2 \times 10^5$ and $\mathrm{Re} = 2 \times 10^6$, where the Reynolds number was varied with changing the viscosity of the fluid inside the computational setup. To ensure accurate representation of fluxes across the domain, C-type hexahedral mesh was generated around the airfoil surface consisting of 2×10^5 cells. The mesh was clustered behind the airfoil to fully capture the von karman vortex sheet. The $y^+ < 1$ was used to resolve the boundary layer until the viscous sub layer. The airfoil is placed inside the domain at a location 20c from the outlet and 10c from the upper and lower surface to avoid the effects from the boundary of domain(where c is the chord length). The boundary condition are kept the same as the previous cylinder case to ensure consistency of the numerical simulations.

4. Results and discussion

The data for each simulation, representing in each case at least one principal period, sampled at 20 Hz, was interpolated on a uniform rectilinear grid measuring 400×200 elements, with a gridsize of $0.1D$. The interpolation step is necessary in the more general setting when snapshots may be defined on different meshes, which is not the case in the present work. Nevertheless, it simplifies the analysis somewhat, as the covariance function $\langle \cdot, \cdot \rangle_a$, which involves a spatial integral, may be computed more easily. From the authors' experience, such an interpolation has negligible impact on the energy spectrum.

The results regarding the energy spectra can be observed in Fig. 1. In all cases, about 30 modes suffice to cover about 95% of the energy content. In some cases, notably the low Reynold's number cases, the number of modes required is considerably fewer—three.

We also note that the energy decay appears roughly consistent among the four cases of mid-high Reynold's number (the red and green lines in Fig. 1), which suggests that this rate of decay might be representative for a wider range of Reynold's numbers and inflow boundary conditions.

Contour plots for the absolute velocity $\|\boldsymbol{v}\|$ of the first three modes in each of the *steady* cases can be seen in Fig. 2. In each case, the principal mode can be seen to be "laminar" in nature, while the second and third modes provide the two phase-shifted principal oscillations directly behind the cylinder (at least, for the low and medium Reynold's number cases). Higher modes provide the more turbulent components. It stands to reason that three modes should suffice for low Reynold's number cases, where there aren't many effects other than "laminar" flow with vortex shedding.

For comparison, the results from the NACA 0015 cases are shown in Figs. 3 and 4, and they show a considerably higher energy content in the first modes than the cylinder cases do, as well as a remarkable similarity across the different Reynolds numbers.

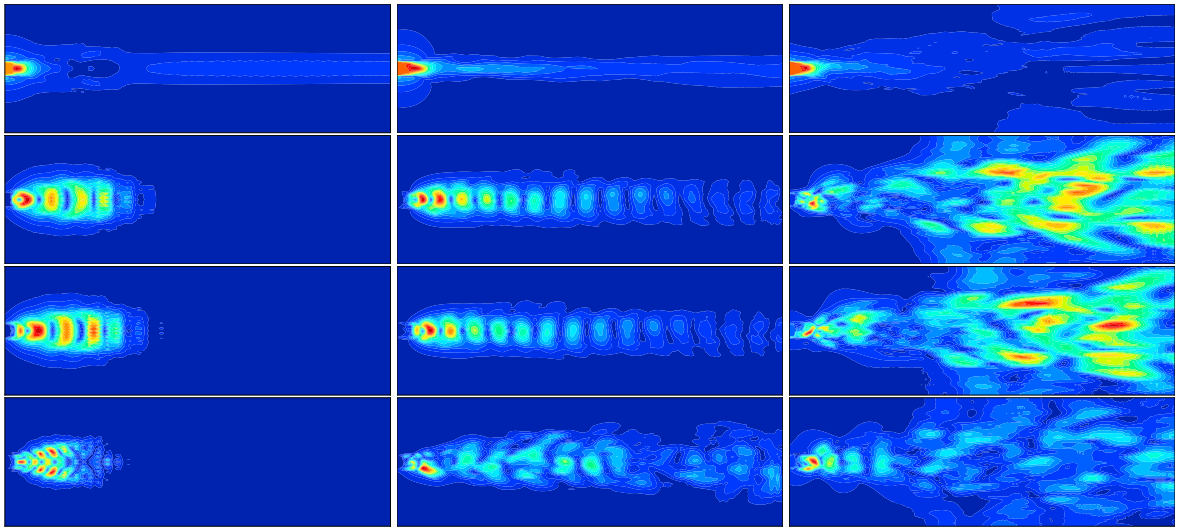

Fig. 2. The first three modes of the steady cylinder cases (Re = 265 on the left, Re = 2580 in the middle and Re = 40000 on the right).

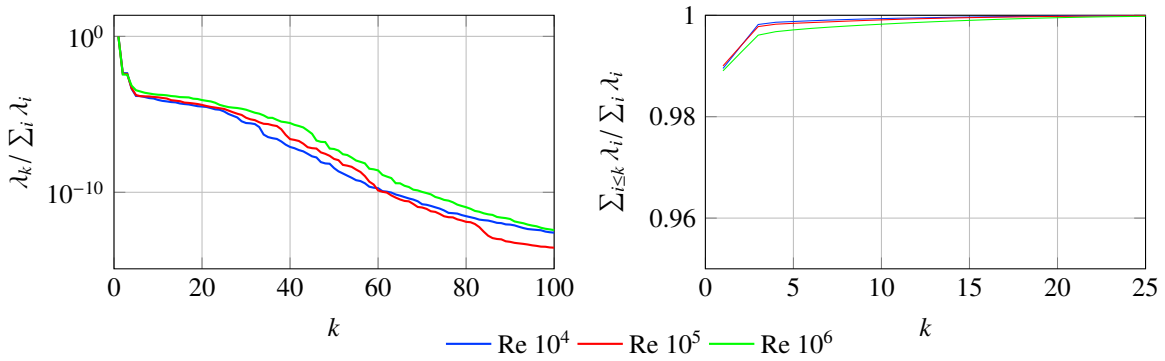

Fig. 3. Energy spectra (on the left, up to 100 eigenvalues) and cumulative energy spectra (on the right, up to 25 eigenvalues) of the NACA 0015 cases. Note the scales on the vertical axis.

5. Conclusion and future work

It can be concluded that for the kind of flows we simulated, POD appears to be an attractive method for constructing the reduced bases required in ROM. In future we intend to build upon the tools and modules presented in this paper to develop computationally efficient tools that can be used on a personal computer. However, there are challenges associated with stability of reduced-order linearized CFD models based on POD [10] that need to be addressed first.

The modular design of the workflow ensures that users can replace any module with their own custom module. For example, in the current work, we used OpenFOAM to generate the snapshots. However, we plan to replace it by our indigenous code IFEM (Isogeometric Finite Element Model [11]) developed within the FSI-WT project (www.fsi-wt.no). This will enable us to utilize snapshots involving airfoils [12,13] and fluid-structure interactions [14] created in the past and demonstrate a wider applicability of the method. Since the most common output format from OF and IFEM is VTK, a format which is not supported by the OpenDAP server, we also need to do a trivial exercise of coverting our existing database invluding VTK into HDF5 format.

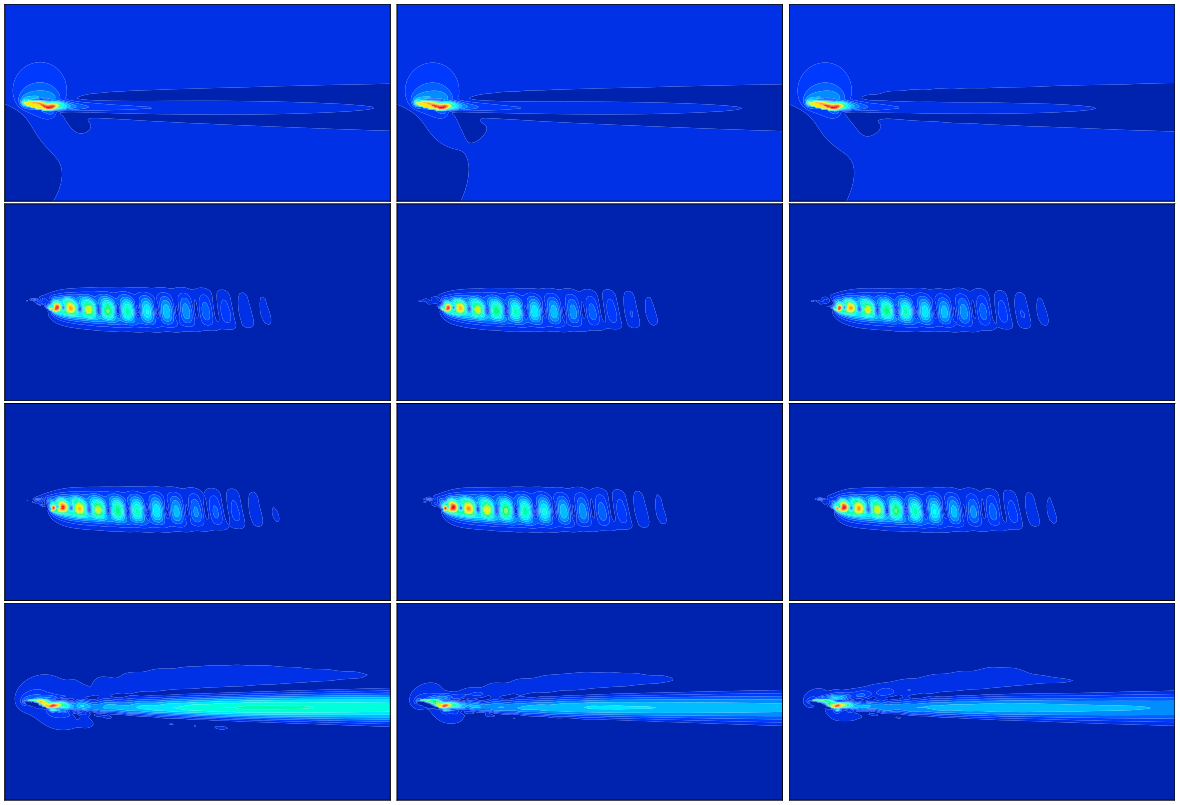

Fig. 4. The first three modes of the NACA 0015 cases (Re = 2×10^4 on the left, Re = 2×10^5 in the middle and Re = 2×10^6 on the right).

Acknowledgements

The authors acknowledge the financial support from the Norwegian Research Council and the industrial partners of FSI-WT (grant no: 216465/E20) (http://www.fsi-wt.no) project.

References

[1] Quarteroni, A., and Rozza, G., eds., 2014. *Reduced Order Methods for Modeling and Computational Reduction*, 1st ed., Vol. 9 of *Modeling, Simulation & Applications*. Springer, Springer International Publishing Switzerland, chap. 8, pp. 235–274.

[2] Tabib, M., Rasheed, A., and Fuchs, F., 2016. "Analyzing complex wake-terrain interactions and its implications on wind-farm performance". *Journal of Physics Conf. Series,* ***753***(032063), Oct.

[3] Tabib, M., Rasheed, A., and Kvamsdal, T., 2015. "Investigation of the impact of wakes and stratification on the performance of an onshore wind farm". *Energy Procedia,* ***80***, pp. 302–311.

[4] Tabib, M., Rasheed, A., and Kvamsdal, T., 2015. "LES and RANS simulation of onshore bessaker wind farm: analyzing terrain and wake effects on wind farm performance". *Journal of Physics Conf. Series,* ***625***(012032).

[5] Siddiqui, S., Rasheed, A., Tabib, M., and Kvamsdal, T., 2016. "Numerical analysis of the nrel 5mw wind turbine: A study towards a better understanding of wake dynamics and torque generation mechanism". *Journal of Physics Conf. Series,* ***753***(032059), Oct.

[6] Rasheed, A., Holdahl, R., Kvamsdal, T., and Åkervik, E., 2014. "A comprehensive simulation methodology for fluid-structure interaction of offshore wind turbines". *Energy Procedia,* ***53***(C), pp. 135–145.

[7] Barbi, C., Favier, D., Maresca, C., and Telionis, D., 1986. "Vortex shedding and lock-on of a circular cylinder in oscillatory flow". *Journal of Fluid Mechanics,* ***170***, pp. 527544.

[8] NA, ed., 2017. Analysis of unsteady hydrodynamics related to vortex induced vibrations on bluff-bodies offshore structures, Submitted to 36th International Conference on Ocean, Offshore and Arctic Engineering.

[9] Liang, C., and Papadakis, G., 2007. "Large eddy simulation of pulsating flow over a circular cylinder at subcritical reynolds number.". *Computers and Fluids,* ***36***, pp. 299–312.

[10] Quarteroni, A., and Rozza, G., eds., 2014. *Reduced Order Methods for Modeling and Computational Reduction*, 1st ed., Vol. 9 of *Modeling, Simulation & Applications*. Springer, Springer International Publishing Switzerland, chap. 8, pp. 215–234.

[11] Opstal, T., Fonn, E., Kvamsdal, T., Kvarving, A., Mathisen, K., Nordanger, K., Okstad, K., Rasheed, A., and Tabib, M., 2015. "Isogeometric methods for CFD and FSI-simulation of flow around turbine blades". *Energy Procedia,* ***80***, pp. 442–449.

[12] Nordanger, K., Holdahl, R., Kvarving, A., Rasheed, A., and Kvamsdal, T., 2015. "Comparison of three isogeometric incompressible navier-stokes solvers applied to simulation of flow past a fixed NACA0012 airfoil". *Computer Methods in Applied Mechanics and Engineering,* ***284***, Feb, pp. 664–688.

[13] Nordanger, K., Holdahl, R., Kvamsdal, T., Kvarving, A., and Rasheed, A., 2015. "Simulation of airflow past a 2D NACA0015 airfoil using an Isogeometric incompressible Navier-Stokes solver with the Spalart-Allmaras turbulence model". *Computer Methods in Applied Mechanics and Engineering,* ***290***, Feb, pp. 183–208.

[14] Nordanger, K., Rasheed, A., Okstad, K., Kvarving, A., Holdahl, R., and Kvamsdal, T., 2016. "Numerical benchmarking of fluid-structure interaction: An isogeometric finite element approach". *Ocean Engineering,* ***124***, pp. 324–339.